

# SACNet: A Spatially Adaptive Convolution Network for 2D Multi-organ Medical Segmentation

Lin Zhang, Wenbo Gao, Jie Yi, Yunyun Yang\*

School of Science

Harbin Institute of Technology, Shenzhen

Shenzhen, China

23s058005@stu.hit.edu.cn, 23B358001@stu.hit.edu.cn, tomatosquid@163.com, yangyunyun@hit.edu.cn

**Abstract**—Multi-organ segmentation in medical image analysis is crucial for diagnosis and treatment planning. However, many factors complicate the task, including variability in different target categories and interference from complex backgrounds. In this paper, we utilize the knowledge of Deformable Convolution V3 (DCNv3) and multi-object segmentation to optimize our Spatially Adaptive Convolution Network (SACNet) in three aspects: feature extraction, model architecture, and loss constraint, simultaneously enhancing the perception of different segmentation targets. Firstly, we propose the Adaptive Receptive Field Module (ARFM), which combines DCNv3 with a series of customized block-level and architecture-level designs similar to transformers. This module can capture the unique features of different organs by adaptively adjusting the receptive field according to various targets. Secondly, we utilize ARFM as building blocks to construct the encoder-decoder of SACNet and partially share parameters between the encoder and decoder, making the network wider rather than deeper. This design achieves a shared lightweight decoder and a more parameter-efficient and effective framework. Lastly, we propose a novel continuity dynamic adjustment loss function, based on t-vMF dice loss and cross-entropy loss, to better balance easy and complex classes in segmentation. Experiments on 3D slice datasets from ACDC and Synapse demonstrate that SACNet delivers superior segmentation performance in multi-organ segmentation tasks compared to several existing methods.

**Index Terms**—Multi-organ segmentation, Adaptive spatial aggregation, Category balancing

## I. INTRODUCTION

Multi-organ medical image segmentation, which simultaneously provides clearer visualization of anatomical and pathological structures across multiple organs, greatly enhances the efficiency and accuracy of diagnosis [1]- [2].

However, it remains challenging due to the following difficulties: (1) Variability in different target categories. As shown in Fig. 1, not only do different organs in the same slice dataset vary significantly in size, shape, and texture, but different slices of the same organ also differ greatly. This variability makes it difficult for segmentation models to generalize effectively, as they may overfit to specific features seen during training and struggle with unseen morphological variations. (2) Interference from complex backgrounds. Fig. 1 shows the complexity of the surrounding anatomical structures and

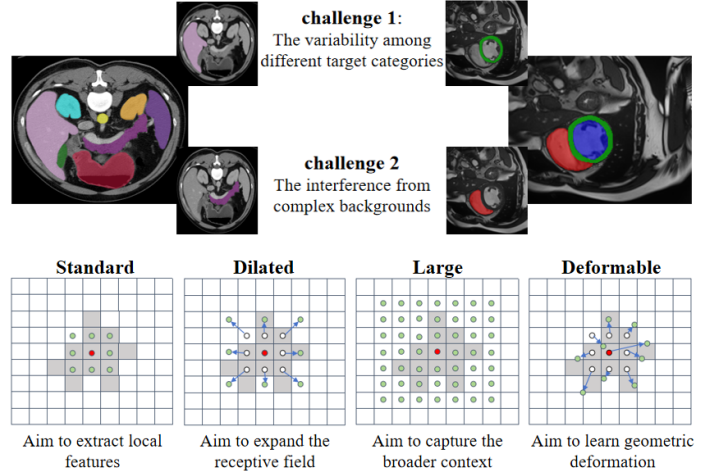


Fig. 1: Overview of challenges in multi-organ segmentation tasks and the effect of different convolutional techniques. The above figure: challenges faced in multi-organ segmentation tasks. The four images below: effects of standard convolutional kernel, dilated convolutional kernel, large-kernel convolutional kernel, and standard deformable convolutional kernel.

the presence of varying textures, intensities, and overlapping tissues, which introduce substantial difficulties. These intricate backgrounds can lead to ambiguous boundaries and obscure the precise contours of the target organs. Consequently, the model’s ability to precisely identify and segment the organs is compromised, often resulting in incomplete or inaccurate segmentation outcomes.

Recently, most existing studies [3]- [16] have utilized standard convolutional kernels, dilated convolutional kernels, large-kernel convolutional kernels, transformers, or hybrid methods as building blocks to design specific network architectures to improve segmentation accuracy. As shown in Fig. 1, dilated and large-kernel convolutional kernels have a larger receptive field compared to standard convolutional kernels. The transformers [9] capture long-range dependencies more effectively through self-attention mechanisms. However, due to significant differences between different organs, these models lack an inherent mechanism to adjust the specific receptive field according to different segmentation targets, in-

\*Corresponding author. This work is supported by National Natural Science Foundation of China [No. 62371156] and Natural Science Foundation of Guangdong Province [No. 2022A1515011629]

evitably losing the perception of the corresponding structures. In this context, some researchers [17]- [20] have started to introduce deformable convolutions and deformable attention transformers for multi-organ medical image segmentation. However, deformable convolutions [17] have limited flexibility in sampling points and high computational complexity. Deformable attention transformers [19] perform poorly when handling imbalanced label data, and the need for large amounts of data for generalization poses significant challenges for medical image tasks, where data is relatively scarce. Some researchers have also attempted to improve loss functions to better adapt to multi-organ medical image segmentation tasks. The standard Dice loss, due to cosine similarity’s disregard for data distribution characteristics [26], treats each class equally, which tends to result in imbalanced segmentation. Various loss functions [21]- [26] based on dice loss have been proposed to further reinforce the stringent constraints on segmentation. Building on this foundation, structured losses combined with continuous dynamic adjustment mechanisms will potentially further improve the accuracy of segmentation.

To tackle the above obstacles, we propose a novel framework, SACNet, involving an Adaptive Receptive Field Module (ARFM), widenet strategy, and dynamic continuity adjustment loss function. (1) To address the variability in different target categories and the interference from complex backgrounds, we propose the ARFM, which combines DCNv3 with a series of tailored block-level and architecture-level designs similar to transformers to enhance the perception of the geometric structure by adaptively focusing on different segmentation targets. Consider that DCNv3 allows the network to freely learn geometrical changes, which can cause perceptual regions to wander; therefore, our ARFM adopts the strategy of grouped convolutions. It divides the bias generation process of DCNv3 into groups corresponding to the segmentation target categories, with each group adaptively adjusting the receptive field according to different targets. Additionally, ARFM introduces the Feed-Forward block to capture specific patterns in the different segmentation targets. It also introduces the Layer Scale block and the DropPath block to prevent the model from excessively freely learning geometric changes. (2) To address the challenge of high memory and computation complexity, we adopt the WideNet strategy [31]. We share the DCNv3 block projection weights of ARFM modules between the encoder and decoder when generating the original location-aware modulation scalars and offsets. Through the FFN block, SACNet can train more parameters in width; by sharing parameters between DCNv3 blocks, SACNet can train fewer parameters in depth. In this method, the network goes wider instead of deeper, achieving a shared lightweight decoder and a more parameter-efficient and effective framework. (3) To address the problem of imbalanced segmentation caused by imbalanced label data, we propose a novel Continuity Dynamic Adjustment Loss Function (CTLoss). Based on t-vMF Dice loss and cross-entropy loss, CTLoss adaptively adjusts using the Intersection Over Union (IOU) of each segmentation category on the validation set after each epoch. Our CTLoss

automatically adjusts to use more compact similarities for easy classes and wider similarities for difficult classes during training.

To summarize, our contributions are as follows:

- We propose an Adaptive Receptive Field Module to enhance the perception of geometric structures by adaptively focusing on different segmentation targets.
- We design a novel convolutional network that expands the network’s width rather than its depth, achieving a shared lightweight decoder and a more parameter-efficient and effective framework.
- We propose a novel continuity dynamic adjustment loss function based on IOU, which better balances easy classes and difficult classes.
- Our proposed SACNet method achieves state-of-the-art performance on two different multi-organ medical image segmentation datasets, as demonstrated by various ablation studies highlighting its effectiveness.

## II. RELATED WORK

### A. Methods based on Network Design

Various methods [3]- [16] have been proposed to achieve better performance by designing specific network structures and modules for multi-organ segmentation. (1) Methods based on the convolutional kernel and transformers: Since the introduction of UNet [3], Convolutional Neural Networks (CNNs) have become the most common choice. To enhance the limited receptive field, researchers [5] have attempted to replace standard convolutions with dilated convolutions and large-kernel convolutions. With the success of vision transformers, TransUNET [9] and similar methods [10]- [12] integrate transformers with convolutions as building blocks for the encoder. SwinUNet [13] and similar methods [14]- [16] aim to create a fully transformer-based model. (2) Methods based on deformable convolution and deformable transformers: Recently, deformable convolutions have been applied to medical image segmentation [17]- [18]. [27] extended standard deformable convolutions to DCNv2, and DCNv3 [28] further enhanced feature extraction at different scales by building on DCNv2. AgileFormer [20] introduced the deformable attention transformer, integrating deformable convolutions into patch embedding, self-attention, and positional encoding within the model. Considering the limitations of convergence difficulty and perceptual region wander caused by excessive randomness, our work integrates the knowledge of deformable convolution v3 and designs the ARFM as a building block for the encoder. The ARFM can adaptively adjust the receptive field according to different segmentation targets and mitigate the excessive flexibility of DCNv3, stably enhancing the perception of different segmentation regions in the feature extraction process.

### B. Methods based on Loss Function

In recent studies, various loss functions based on Dice loss have been proposed to further improve the Dice Similarity Coefficient (DSC) [21]- [25]. Li et al. [21] proposed

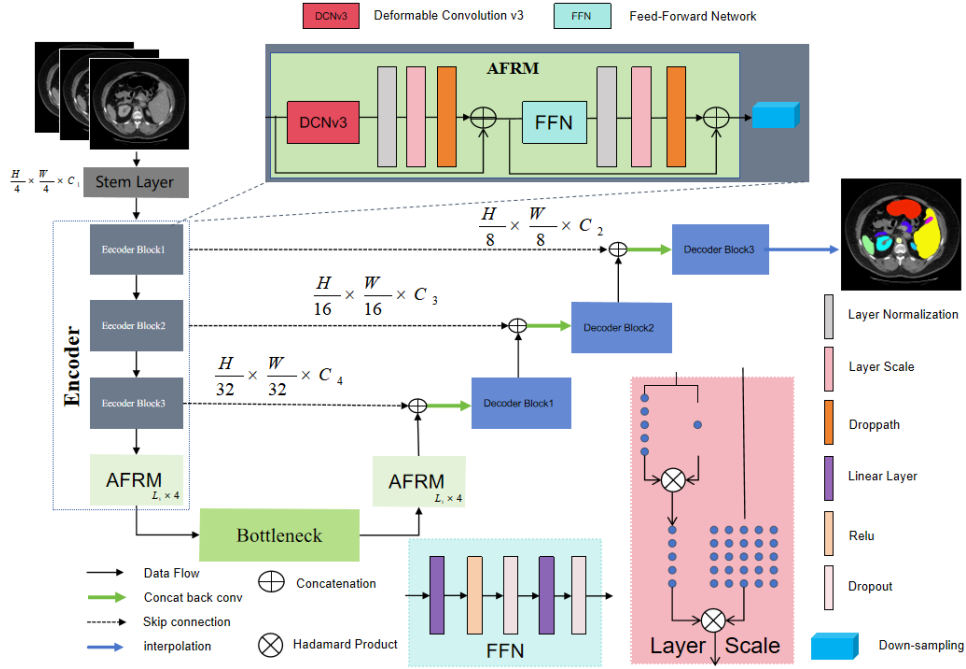


Fig. 2: Overview of the SACNet architecture. The left side of the network represents the encoder, which uses four stages of adaptive spatial aggregation feature extraction, while the right side shows the shared lightweight decoder that generates the segmentation maps. Each block of the ARFM employs pre-trained DCNv3 that adaptively aggregates spatial features. The Feed-Forward block captures specific patterns in the different segmentation targets and introduces the Layer Scale block and the DropPath block to prevent the model from excessively freely learning geometric changes.

a generalized Dice loss that utilizes the class re-balancing properties of the generalized Dice overlap, achieving a robust and accurate deep learning loss function for unbalanced segmentation. Shit et al. [22] introduced a similarity measurement termed centerline Dice, which is calculated based on the intersection of the segmentation masks and the skeleton. Wang et al. [23] improved Dice loss by mining the information of negative areas. Kato and Hotta [25] applied the t-vMF similarity to the Dice loss, adjusting the compactness of the similarity for each class. Drawing inspiration from this, our work proposes a novel Continuity Dynamic Adjustment Loss Function (CTLoss), which combines t-vMF dice loss and cross-entropy loss. Our CTLoss introduces a new dynamic updating mechanism, updating with the average IOU of each class on the validation set after each epoch, better guiding the network to balance easy classes and difficult classes.

### III. METHOD

#### A. Encoder

Recent advancements in large-scale models [27] based on Convolutional Neural Networks (CNNs) have shown the potential of Deformable Convolution v3 (DCNv3), which has demonstrated greater effectiveness in various downstream visual tasks. In our SACNet model, we primarily utilize the ARFM module, which employs the pre-trained DCNv3 block as its core operation. This module integrates the DCNv3 block with a series of tailored block-level and architecture-

level designs similar to Transformers to serve as the building blocks of the spatially adaptive pyramid feature encoder. Specifically, our input is an image size of  $3 \times 224 \times 224$ , starting with a Stem Layer, which applies convolution followed by layer normalization and activation functions. Next, the input passes through four stages with embedding sizes of 112, 224, 448, and 896, respectively. Each stage consists of a different number of ARFM modules and a down-sampling module, with each ARFM module composed of five separate blocks: the DCNv3 block, which provides the model with the capability to adjust specific adaptive receptive fields according to different segmentation targets; the Layer Norm block, which performs normalization on the input samples; the Feed-Forward block, which captures specific patterns in the different segmentation targets; the Layer Scale block and DropPath block, which prevent the model from excessively freely learning geometric changes. The implementation of ARFM is shown in Equations (1)-(3) as follows:

$$DCN(p_0) = \sum_{g=1}^G \sum_{k=1}^K w_g m_{gk} x_g(p_0 + p_k + \Delta p_{gk}), \quad (1)$$

$$z'_l = DP(\gamma_1 \cdot N(DCN(z_{l-1})) + z_{l-1}), \quad (2)$$

$$z_l = DP(\gamma_2 \cdot N(FFN(z'_l)) + z'_l), \quad (3)$$

where  $K$  represents the total number of sampling points, and  $k$  enumerates each sampling point.  $G$  denotes the total number

of aggregation groups. For the  $g$ -th group,  $\mathbf{w}_g \in \mathbb{R}^{C' \times C'}$  represents the location-irrelevant projection weights, where  $C' = \frac{C}{G}$  defines the group dimension.  $m_{gk} \in \mathbb{R}$  denotes the modulation scalar of the  $k$ -th sampling point in the  $g$ -th group, normalized by the softmax function along dimension  $K$ .  $\mathbf{x}_g \in \mathbb{R}^{C' \times H \times W}$  represents the sliced input feature map.  $p_k$  denotes the  $k$ -th location of the pre-defined grid sampling  $\{(-1, -1), (-1, 0), \dots, (0, +1), \dots, (+1, +1)\}$  as in regular convolutions.  $\Delta p_{gk}$  is the offset corresponding to the grid sampling location  $p_k$  in the  $g$ -th group. *DCN* stands for deformable convolution v3.  $\gamma_1$  and  $\gamma_2$  are the inter-layer scaling factors,  $N$  denote layer normalization, and *DP* denotes the droppath function.

The third layer of the encoder typically captures better feature representations than the others [28]. Through extensive experiments, we ultimately distribute more computation to the third encoder stage with an ARFM module ratio of [4, 4, 21, 4], respectively. A skip connection is utilized inside each stage to address the issue of vanishing gradients and facilitate information flow. Our encoder generates four feature representations of size  $\{1 \times (112 \times 2^i) \times \frac{H}{2^{2+i}} \times \frac{W}{2^{2+i}}\}$  in four different stages where  $i = \{0, 1, 2, 3\}$ , which are passed to the decoder through skip connections. All modules are connected in the sequence shown in Fig. 2.

### B. Decoder

The SACNet decoder has four consecutive decoder blocks and one bottleneck block. Each decoder block starts with layer normalization, and then upsamples the inputs by a factor of two to match the size of the encoder outputs. Next, we apply the ARFM module to reshape the features, followed by layer normalization while keeping the input dimension the same. We then concatenate it with the encoder output through the skip connection. Similar to regular convolution, when the DCNv3 block generates offsets  $\Delta p_{gk}$  and modulation scalars  $m_{gk}$ , different convolutional neurons in different groups have independent linear projection weights. Therefore, as the total number of sampling points increases, the model's parameter and memory complexity grow rapidly, significantly limiting the model's efficiency. To address this problem, we borrow the idea from WideNet [31], which shares some model parameters in depth. We share the DCNv3 block projection weights of ARFM modules between the encoder and decoder when generating the original location-aware modulation scalars and offsets. Through the Feed-Forward blocks, SACNet can train more parameters in width; by sharing parameters between DCNv3 blocks, SACNet can train fewer parameters in depth. Then, we apply bilinear interpolation to resize the images to  $H \times W \times N$ , where  $N$  is the number of classes, used as the final segmented maps of the decoder, and pass through Softmax to classify each pixel. The operation of the bottleneck layer is the same as the other four decoder blocks, except that the bottleneck gathers more information in the channel of the image while the image size remains the same. Additionally, our decoder does not incorporate any extra techniques or strategies such as residual connections [29] or deep supervision [30].

### C. Model Architectures

The overall architecture of our model is illustrated in Fig. 2. Like most medical image segmentation modeling methods [8]–[10], an encoder-decoder design is employed. Our framework contains four stages of adaptive spatial aggregation feature extraction encoders and a shared lightweight decoder. For an input RGB medical image with the shape of  $H \times W \times 3$ , we first use stem layers to reduce the spatial resolution. Subsequently, four feature maps ( $X_1$ ,  $X_2$ ,  $X_3$ , and  $X_4$ ) in four different stages are generated and concatenated with the up-sampled features of the decoder through skip connections. The extracted features from the last stage ( $X_4$ ) are also passed through a bottleneck layer, where the channel size is adjusted to gather more information while keeping the image size the same. The features from the bottleneck layer are propagated upward, up-sampled by a scale of two, and concatenated with the features from the encoder. We apply bilinear interpolation to generate the final segmentation maps, which pass through a softmax layer to classify each pixel.

### D. Training Loss

Recent 2D medical image segmentation methods combine the Dice loss with the cross-entropy loss as the final loss function. However, for multi-object segmentation tasks, the standard Dice loss, due to cosine similarity's disregard for data distribution characteristics [25], treats each class equally, which tends to result in imbalanced segmentation. In this study, we tested most of the proposed loss functions for multi-class medical image segmentation and comprehensively considered the loss aggregation strategy. We propose a novel Continuity Dynamic Adjustment Loss Function (CTLoss) based on t-vMF Dice loss [25] and the cross-entropy loss function. This new loss function adaptively uses more compact similarities for easy classes and wider similarities for difficult classes, making it more effective in helping the model converge better and more efficiently for multi-object image segmentation.

The t-vMF Dice Loss is formulated as:

$$\cos \theta_i = \sum_{i=1}^n A_{in} B_{in}, \quad (4)$$

$$\phi_\kappa(\cos \theta; \kappa) = \frac{1 + \cos \theta}{1 + \kappa(1 - \cos \theta)} - 1, \quad (5)$$

$$L_{t-vMF} = \frac{1}{C} \sum_{i=1}^C (1 - \phi_\kappa(\cos \theta_i; \kappa))^2, \quad (6)$$

where  $n$  indicates the number of class samples,  $i$  represents the category index,  $A_{in}$  indicates the vectors containing all positive examples predicted by the model, and  $B_{in}$  indicates the vectors containing all positive examples of the ground truth in the dataset.  $\kappa$  is a concentration parameter that adjusts the shape of the similarity function, and  $C$  is the number of classes. We propose an effective algorithm that uses the Intersection Over Union (IOU) of the model on the validation set to update  $\kappa$  in the t-vMF Dice loss after each epoch. This approach adaptively determines  $\kappa$  to achieve more compact

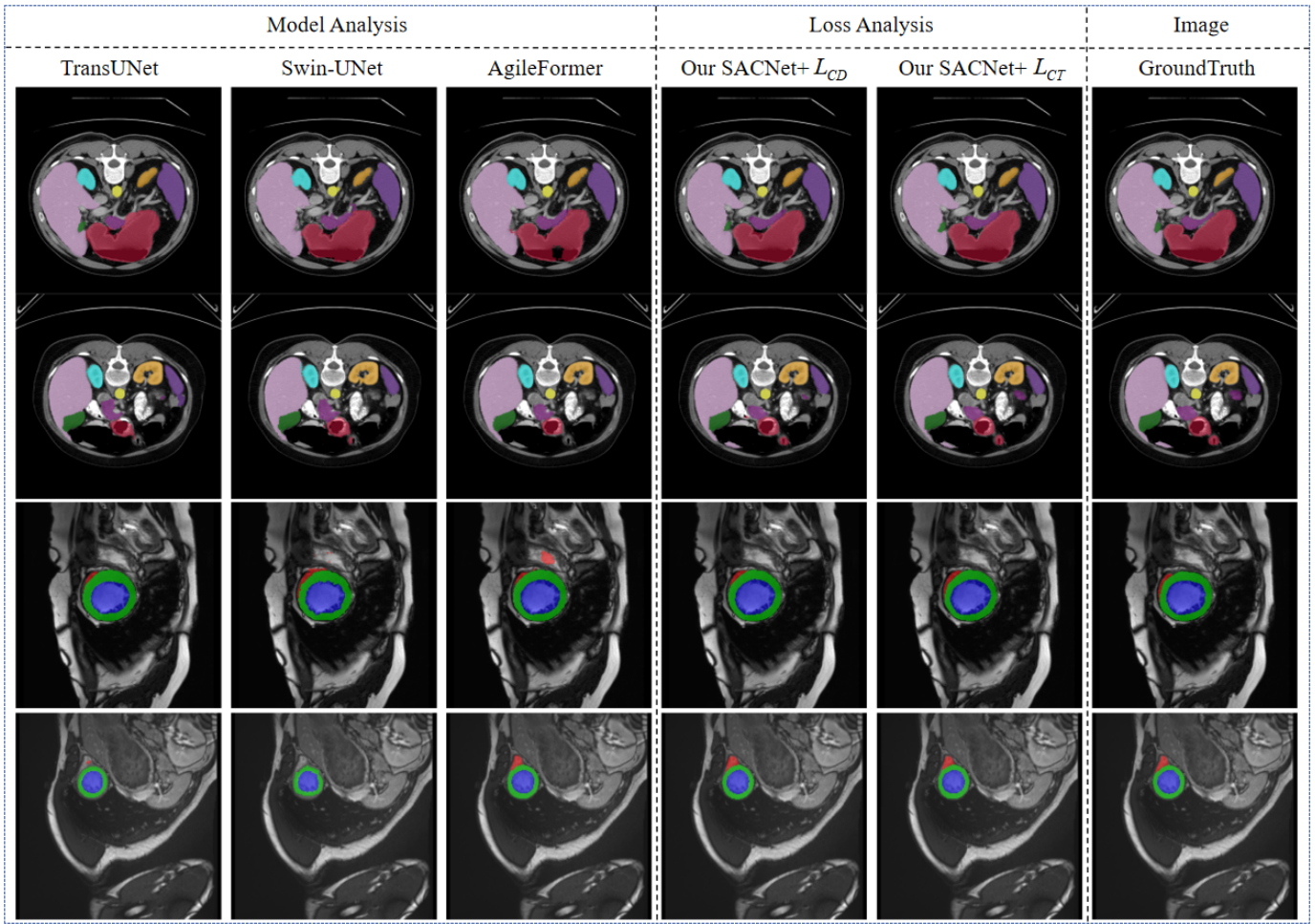


Fig. 3: Qualitative comparisons of the segmentation performance of our approach alongside other segmentation methods. The first and second rows show the results of the Synapse dataset, where the color codes are: yellow for the aorta, green for the gallbladder, orange for the left kidney, cyan for the right kidney, plum for the liver, purple for the pancreas, indigo for the spleen, and crimson for the stomach. The third and fourth rows show the results of the ACDC dataset, where the color codes are: red for the right ventricle, green for the myocardium, and blue for the left ventricle. From left to right, we show the results from TransUNet, Swin-UNet, AgileFormer, our SACNet with  $L_{CD}$  (a combination of cross-entropy loss and Dice loss), our SACNet with  $L_{CT}$  (our proposed dynamic loss), and the ground truth.

similarities for easy classes and wider similarities for difficult classes.

The multi-class cross-entropy loss function is defined as follows:

$$L_{CE} = - \sum_{i=1}^N \sum_{c=1}^C y_{ic} \log(\hat{y}_{ic}), \quad (7)$$

where  $N$  represents the total number of samples, and  $C$  is the total number of classes.  $y_{ic}$  denotes the true label for sample  $i$  and class  $c$  (if the sample belongs to class  $c$ , then  $y_{ic} = 1$ , otherwise  $y_{ic} = 0$ ).  $\hat{y}_{ic}$  is the predicted probability that sample  $i$  belongs to class  $c$ .

The final loss function combines the adaptive t-VMF Dice Loss and the cross-entropy loss:

$$L_{CT} = \gamma L_{t-VMF} + (1 - \gamma) L_{CE}, \quad (8)$$

where  $\gamma$  is the weight coefficient, with  $\gamma = 0.6$  and  $1 - \gamma = 0.4$  representing the weights for the adaptive t-VMF Dice loss and the cross-entropy loss, respectively.

## IV. EXPERIMENT

### A. Dataset

Consistent with previous work, we validated the proposed method on two public medical image segmentation datasets: the Synapse multi-organ segmentation dataset and the Automated Cardiac Diagnosis Challenge (ACDC) dataset.

The Synapse dataset consists of 30 scans of eight abdominal organs from the MICCAI 2015 Multi-Atlas Abdominal Labeling Challenge. These eight organs include the left kidney, right kidney, aorta, spleen, gallbladder, liver, stomach, and pancreas. There are a total of 3779 axially enhanced abdominal clinical CT images. Following previous studies, we report the mean

TABLE I: Comparative analysis of model performance with 2D methods in multi-organ segmentation using the synapse dataset. The best result within each column is highlighted in bold, and the second-best is underlined. Models marked with an asterisk (\*) were implemented by us.

Model	Year	Aorta	Gallbladder	Kidney(L)	Kidney(R)	Liver	Pancreas	Spleen	Stomach	Average	
										DSC $\uparrow$	HD95 $\downarrow$
U-net [3]	2015	<b>89.07</b>	69.72	77.77	68.6	93.43	53.98	86.67	75.58	76.85%	39.70
U-Net++ [4]	2018	88.19	68.89	81.76	75.27	93.01	58.20	83.44	70.52	76.91%	36.93
MultiResUNet [5]	2020	87.33	65.67	82.08	73.82	93.68	52.85	85.23	75.66	77.42%	36.84
TransUNet [9]	2021	87.23	63.13	81.87	77.02	94.08	55.86	85.08	75.62	77.48%	31.69
TransNorm [10]	2022	86.16	65.11	82.18	78.64	93.42	55.34	89.50	76.01	78.40%	30.25
Swin-UNet [13]	2022	85.47	66.53	83.28	79.61	94.29	56.58	90.66	76.60	79.13%	21.55
DA-TransUNet* [11]	2023	87.13	58.75	79.39	78.41	94.82	62.62	87.84	79.72	78.59%	29.20
DAE-Former [16]	2023	88.96	<b>72.30</b>	86.08	80.88	94.98	65.12	<u>91.94</u>	79.19	82.43%	17.46
ParaTransCNN [12]	2024	88.12	68.97	<u>87.99</u>	<u>83.84</u>	95.01	69.79	<b>92.71</b>	84.43	83.86%	<u>15.86</u>
AgileFormer* [20]	2024	88.52	70.37	85.69	81.14	95.65	<b>70.78</b>	91.19	86.17	83.69%	19.37
SACNet+ $L_{CD}$ (Ours)	2024	88.46	71.05	83.68	80.99	<u>95.74</u>	<b>71.40</b>	91.27	<u>86.56</u>	83.64%	22.01
SACNet+ $L_{CT}$ (Ours)	2024	<u>88.88</u>	<u>70.45</u>	<b>89.36</b>	<b>85.41</b>	<b>95.98</b>	<u>70.38</u>	91.26	<b>87.64</b>	<b>84.92%</b>	<b>15.13</b>

Dice Similarity Coefficient (DSC) and the 95% Hausdorff Distance (HD95) for the segmentation of abdominal organs using 18 training cases (2212 axial slices) and 12 validation cases.

The ACDC dataset consists of cine MR images acquired during breath-hold, covering the heart from the base to the apex of the left ventricle. Each scan was annotated with ground truth for the Left Ventricle (LV), Right Ventricle (RV), and Myocardium (Myo). Following previous studies, we report the mean DSC for 70 training cases (1930 axial slices), 10 validation cases, and 20 test cases.

### B. Evaluation

We evaluate our model’s performance on the ACDC and Synapse multi-organ datasets using the DSC and the HD95 for the Synapse dataset. The DSC and HD95 are calculated according to the formulas as follows:

$$DSC(X, Y) = \frac{2 \cdot |X \cap Y|}{|X| + |Y|}, \quad (9)$$

$$HD95(A, B) = \max \left\{ \max_{a \in A} \min_{b \in B} \|a - b\|, \max_{b \in B} \min_{a \in A} \|b - a\| \right\}, \quad (10)$$

where  $X$  represents the predicted segmentation mask, and  $Y$  represents the ground truth segmentation mask.  $a$  and  $b$  are points in sets  $A$  and  $B$  respectively.  $A$  represents the set of points in the predicted segmentation mask, and  $B$  represents the set of points in the ground truth segmentation mask.

### C. Setups

The model and experiments were implemented using PyTorch 2.2.0 and the CUDA toolkit 12.1, with all experiments conducted on an NVIDIA 3090 24G GPU. To improve computational efficiency, the resolution of all training, validation, and test images was resized to 224×224. We used a batch size of

18, an initial learning rate of  $3 \times 10^{-4}$ , and trained the models for 400 epochs. All models were trained using a combination of t-vMF Dice Loss and cross-entropy losses, incorporating our proposed continuity dynamic adaptive algorithm. The AdamW optimizer was used, employing cosine learning rate decay. For better model initialization, we initialized the model parameters with weights pre-trained on ImageNet-1k. The DSC and the HD95 were used as metrics to evaluate segmentation accuracy. During training, the best validation weights were recorded to test the performance of our model.

TABLE II: Performance comparison with 2D methods in cardiac MRI segmentation using the ACDC dataset. The best result within each column is highlighted in bold, and the second-best is underlined. Models marked with an asterisk (\*) were implemented by us.

Model	Year	RV	Myo	LV	DSC $\uparrow$
R50+UNet [9]	2021	87.10	80.63	94.92	87.55%
TransUNet [9]	2021	86.67	87.27	95.18	89.71%
MISSFormer [14]	2021	89.55	88.04	94.99	90.86%
Swin-UNet [13]	2022	85.77	84.42	94.03	88.07%
MT-UNet [32]	2022	86.64	89.04	95.62	90.43%
TransCASCADE [33]	2023	89.14	90.25	95.50	91.63%
Parallel MERIT [34]	2024	90.87	90.00	96.08	92.32%
AgileFormer* [20]	2024	90.93	<b>90.29</b>	95.99	<u>92.41%</u>
SACNet+ $L_{CD}$ (Ours)	2024	<u>91.05</u>	89.96	<u>96.01</u>	92.34%
SACNet+ $L_{CT}$ (Ours)	2024	<b>91.38</b>	<u>90.11</u>	<b>96.10</b>	<b>92.53%</b>

## V. RESULT

### A. Performance on Synapse Dataset

On the Synapse dataset, as shown in Table I, our SACNet stands out with the highest scores for most organs, achieving

TABLE III: Comparison of Ablation Studies: Only a single parameter is altered while keeping the others constant to observe the impact of each parameter on performance. D represents the DCNv3 block, F represents the FFN block, and S represents the Layer Scale and DropPath block.

D	F	S	CFLoss	Aorta	Gallbladder	Kidney(L)	Kidney(R)	Liver	Pancreas	Spleen	Stomach	DSC↑	HD95↓
	✓	✓	✓	84.33	60.83	85.73	77.54	93.54	50.12	88.20	75.62	76.99%	31.05
✓	✓		✓	85.81	66.21	85.58	81.09	94.98	58.81	92.16	77.12	80.22%	16.90
✓		✓	✓	87.23	64.81	86.97	83.35	94.74	62.50	93.25	81.58	81.81%	15.84
✓	✓	✓		88.46	71.05	83.68	80.99	95.74	71.40	91.27	86.56	83.64%	22.01
✓	✓	✓	✓	88.88	70.45	89.36	85.41	95.98	70.38	91.26	87.64	84.92%	15.13

89.36% for the left kidney, 85.41% for the right kidney, 95.98% for the liver, and 87.64% for the stomach. For other organs, except the spleen, our SACNet also achieves the second-best scores. Additionally, our DSC reaches 84.92% and HD95 is 15.13, both being the best results compared to other benchmarks. Figure 3 provides visual examples of the segmentation outputs produced by our proposed model and other state-of-the-art methods. As shown, our predictions have clearer boundaries between different segmentation targets: the boundaries between the pancreas and spleen are clear and smooth. Our model is more accurate for small objects: Swin-UNet and AgileFormer miss the gallbladder in their segmentations, and TransUNet only partially segments it, but our model segments it completely. As shown in the last two rows of Table I, replacing CDLoss with CTLoss significantly improves the results for DSC and HD95, as well as for most organs, particularly the left and right kidneys. In most slice data, the left and right kidneys have complex boundaries and overlap with surrounding organs, making them relatively difficult to segment, as shown in the orange and cyan regions in Figure 3. This demonstrates that our CTLoss is highly effective in balancing easy and difficult classes.

### B. Performance on ACDC Dataset

On the ACDC dataset, our SACNet outperforms other models in terms of segmentation accuracy. As shown in Table II, our proposed SACNet achieves the best segmentation results compared to other benchmarks, with a Dice score of 92.53%, representing a significant improvement of 4.46% over Swin-UNet and a 2.82% increase over TransUNet. Furthermore, in Figure 3, we provide visual illustrations of the segmentation outputs produced by our proposed model and other state-of-the-art approaches. As demonstrated, our predictions have clearer boundaries between different segmentation targets and align closely with the provided ground truth masks, indicating the effectiveness of our approach. One notable advantage of SACNet is its capability to model adaptive receptive fields according to different segmentation targets. Additionally, the inclusion of our CTLoss results in a significant improvement in segmentation accuracy for difficult classes compared to easy classes, such as the right ventricle. In most slice data, the RV is smaller in volume and has a higher overlap with other organs, making it a difficult class, as shown in the red portion

of Figure 3. This result demonstrates the effectiveness of our loss function in balancing categories.

### C. Ablation Study

Taking the Synapse dataset as an example, we ablate the key components in our SACNet to verify the effectiveness of these designs. As shown in Table III, we evaluate the effectiveness of our pre-trained DCNv3 blocks, FFN blocks, Layer Scale, and DropPath blocks respectively. When these key modules are removed, the model’s performance decreases to varying degrees. Without DCNv3, the model’s DSC drops from 84.92% to 76.99%, and HD95 increases from 15.13 to 31.05, with performance declining the most severely. This demonstrates that DCNv3 plays a vital role in our model. We also compare our model using two different loss functions: one combining cross-entropy and Dice loss, and the other using our proposed continuity dynamic adjustment loss function. The results show that using CTLoss for updating the model achieves better performance, and CTLoss is highly effective in balancing easy classes and difficult classes. Based on our comparisons, it is evident that the ARFM we designed, which integrates pre-trained DCNv3 blocks, FFN blocks, Layer Scale blocks, and DropPath blocks, can significantly enhance accuracy and establish SACNet as a new state-of-the-art model for the 2D multi-organ medical image segmentation task.

## VI. CONCLUSION

In this study, we focus on the 2D multi-organ medical segmentation task and utilize the knowledge of deformable convolution v3 and multi-object segmentation to optimize our SACNet in three aspects: feature extraction, model architecture, and loss constraint, simultaneously enhancing perception for different segmentation targets. Firstly, we propose the Adaptive Receptive Field Module (ARFM), which combines (DCNv3) with a series of customized block-level and architecture-level designs similar to transformers. This module can capture the unique features of different organs by adaptively adjusting the receptive field according to various targets. Secondly, we utilize ARFM as building blocks to construct the encoder-decoder of SACNet and partially share parameters between the encoder and decoder, making the network wider rather than deeper, thereby achieving a more parameter-efficient and effective framework. Lastly, we propose a novel continuity

dynamic adjustment loss function, based on t-vMF Dice loss and cross-entropy loss, to better balance easy and complex classes in segmentation. Our method is verified on 3D slice datasets from ACDC and Synapse, and the results show that our method provides better accuracy in multi-organ segmentation tasks compared to several existing methods.

However, there are limitations to our work compared to 3D segmentation methods. 3D segmentation can utilize the complete information from volumetric data, providing higher accuracy, but its computational and memory complexity is also significantly higher. In the future, we aspire to extend our method to 3D segmentation tasks to further enhance performance.

## REFERENCES

- [1] R. Wang, T. Lei, R. Cui, et al., "Medical image segmentation using deep learning: A survey," *IET Image Processing*, vol. 16, no. 5, pp. 1243-1267, 2022.
- [2] X. Liu, L. Song, S. Liu, et al., "A review of deep-learning-based medical image segmentation methods," *Sustainability*, vol. 13, no. 3, p. 1224, 2021.
- [3] O. Ronneberger, P. Fischer, and T. Brox, "U-net: Convolutional networks for biomedical image segmentation," in *Proc. Medical Image Computing and Computer-Assisted Intervention (MICCAI)*, Munich, Germany, 2015, pp. 234-241.
- [4] Z. Zhou, M. M. R. Siddiquee, N. Tajbakhsh, et al., "Unet++: A nested u-net architecture for medical image segmentation," in *Proc. Deep Learning in Medical Image Analysis and Multimodal Learning for Clinical Decision Support (DLMIA)*, Granada, Spain, 2018, pp. 3-11.
- [5] N. Ibtehaz and M. S. Rahman, "MultiResUNet: Rethinking the U-Net architecture for multimodal biomedical image segmentation," *Neural Networks*, vol. 121, pp. 74-87, 2020.
- [6] Y. Chen, T. Zhou, Y. Chen, et al., "HADNet: Automatic segmentation of COVID-19 infection based on a hybrid attention dense connected network with dilated convolution," *Computers in Biology and Medicine*, vol. 149, p. 105981, 2022.
- [7] X. Shu, Y. Gu, X. Zhang, et al., "FCRB U-Net: A novel fully connected residual block U-Net for fetal cerebellum ultrasound image segmentation," *Computers in Biology and Medicine*, vol. 148, p. 105693, 2022.
- [8] F. Isensee, P. F. Jaeger, S. A. A. Kohl, et al., "nnU-Net: a self-configuring method for deep learning-based biomedical image segmentation," *Nature Methods*, vol. 18, no. 2, pp. 203-211, 2021.
- [9] J. Chen, Y. Lu, Q. Yu, et al., "Transunet: Transformers make strong encoders for medical image segmentation," *arXiv preprint arXiv:2102.04306*, 2021.
- [10] R. Azad, M. T. Al-Antary, M. Heidari, et al., "Transnorm: Transformer provides a strong spatial normalization mechanism for a deep segmentation model," *IEEE Access*, vol. 10, pp. 108205-108215, 2022.
- [11] G. Sun, Y. Pan, W. Kong, et al., "DA-TransUNet: Integrating Spatial and Channel Dual Attention with Transformer U-Net for Medical Image Segmentation," *arXiv preprint arXiv:2310.12570*, 2023.
- [12] H. Sun, J. Xu, and Y. Duan, "ParaTransCNN: Parallelized TransCNN Encoder for Medical Image Segmentation," *arXiv preprint arXiv:2401.15307*, 2024.
- [13] H. Cao, Y. Wang, J. Chen, et al., "Swin-unet: Unet-like pure transformer for medical image segmentation," in *Proc. European Conference on Computer Vision (ECCV)*, Cham, Switzerland: Springer Nature Switzerland, 2022, pp. 205-218.
- [14] X. Huang, Z. Deng, D. Li, et al., "MISSFormer: an effective transformer for 2D medical image segmentation," *IEEE Transactions on Medical Imaging*, 2022.
- [15] R. Azad, M. Heidari, M. Shariatnia, et al., "Transdeeplab: Convolution-free transformer-based deeplab v3+ for medical image segmentation," in *Proc. International Workshop on Predictive Intelligence In Medicine (PRIME)*, Cham, Switzerland: Springer Nature Switzerland, 2022, pp. 91-102.
- [16] R. Azad, R. Arimond, E. K. Aghdam, et al., "Dae-former: Dual attention-guided efficient transformer for medical image segmentation," in *Proc. International Workshop on Predictive Intelligence In Medicine (PRIME)*, Cham, Switzerland: Springer Nature Switzerland, 2023, pp. 83-95.
- [17] J. Dai, H. Qi, Y. Xiong, et al., "Deformable convolutional networks," in *Proc. IEEE International Conference on Computer Vision (ICCV)*, 2017, pp. 764-773.
- [18] H. H. Lee, Q. Liu, Q. Yang, et al., "DeformUX-Net: Exploring a 3D Foundation Backbone for Medical Image Segmentation with Depthwise Deformable Convolution," *arXiv preprint arXiv:2310.00199*, 2023.
- [19] Z. Xia, X. Pan, S. Song, et al., "Vision transformer with deformable attention," in *Proc. IEEE/CVF Conference on Computer Vision and Pattern Recognition (CVPR)*, 2022, pp. 4794-4803.
- [20] P. Qiu, J. Yang, S. Kumar, et al., "AgileFormer: Spatially Agile Transformer UNet for Medical Image Segmentation," *arXiv preprint arXiv:2404.00122*, 2024.
- [21] C. H. Sudre, W. Li, T. Vercauteren, et al., "Generalised dice overlap as a deep learning loss function for highly unbalanced segmentations," in *Proc. Deep Learning in Medical Image Analysis and Multimodal Learning for Clinical Decision Support (DLMIA)*, Québec City, QC, Canada, 2017, pp. 240-248.
- [22] S. Shit, J. C. Paetzold, A. Sekuboyina, et al., "cDice-a novel topology-preserving loss function for tubular structure segmentation," in *Proc. IEEE/CVF Conference on Computer Vision and Pattern Recognition (CVPR)*, 2021, pp. 16560-16569.
- [23] L. Wang, C. Wang, Z. Sun, et al., "An improved dice loss for pneumothorax segmentation by mining the information of negative areas," *IEEE Access*, vol. 8, pp. 167939-167949, 2020.
- [24] P. Wang and A. C. S. Chung, "Focal dice loss and image dilation for brain tumor segmentation," in *Proc. Deep Learning in Medical Image Analysis and Multimodal Learning for Clinical Decision Support (DLMIA)*, Granada, Spain, 2018, pp. 119-127.
- [25] S. Kato and K. Hotta, "Adaptive t-vmf dice loss for multi-class medical image segmentation," *arXiv preprint arXiv:2207.07842*, 2022.
- [26] X. Zhu, H. Hu, S. Lin, et al., "Deformable convnets v2: More deformable, better results," in *Proc. IEEE/CVF Conference on Computer Vision and Pattern Recognition (CVPR)*, 2019, pp. 9308-9316.
- [27] W. Wang, J. Dai, Z. Chen, et al., "Internimage: Exploring large-scale vision foundation models with deformable convolutions," in *Proc. IEEE/CVF Conference on Computer Vision and Pattern Recognition (CVPR)*, 2023, pp. 14408-14419.
- [28] H. Wang, P. Cao, J. Wang, et al., "Uctransnet: rethinking the skip connections in u-net from a channel-wise perspective with transformer," in *Proc. AAAI Conference on Artificial Intelligence (AAAI)*, 2022, vol. 36, no. 3, pp. 2441-2449.
- [29] A. Hatamizadeh, Y. Tang, V. Nath, et al., "Unetr: Transformers for 3d medical image segmentation," in *Proc. IEEE/CVF Winter Conference on Applications of Computer Vision (WACV)*, 2022, pp. 574-584.
- [30] B. Dong, W. Wang, D. P. Fan, et al., "Polyp-pvt: Polyp segmentation with pyramid vision transformers," *arXiv preprint arXiv:2108.06932*, 2021.
- [31] F. Xue, Z. Shi, F. Wei, et al., "Go wider instead of deeper," in *Proc. AAAI Conference on Artificial Intelligence (AAAI)*, 2022, vol. 36, no. 8, pp. 8779-8787.
- [32] H. Wang, S. Xie, L. Lin, et al., "Mixed Transformer U-Net for Medical Image Segmentation," in *Proc. IEEE/CVF Conference on Computer Vision and Pattern Recognition (CVPR)*, 2022, pp. 2390-2394.
- [33] M. M. Rahman and R. Marculescu, "Medical image segmentation via cascaded attention decoding," in *Proc. IEEE/CVF Winter Conference on Applications of Computer Vision (WACV)*, 2023, pp. 6222-6231.
- [34] M. M. Rahman and R. Marculescu, "Multi-scale hierarchical vision transformer with cascaded attention decoding for medical image segmentation," in *Proc. Medical Imaging with Deep Learning (MIDL)*, 2024, pp. 1526-1544.